Journal of Materials Chemistry B

RSC Publishing

PAPER

View Article Online
View Journal | View Issue

Cite this: *J. Mater. Chem. B*, 2013, **1**, 1826

Synthesis of hydroxyapatite–reduced graphite oxide nanocomposites for biomedical applications: oriented nucleation and epitaxial growth of hydroxyapatite†

Yi Liu, Jing Huang and Hua Li*

Received 14th December 2012
Accepted 25th January 2013

DOI: 10.1039/c3tb00531c

www.rsc.org/MaterialsB

Regardless of its successful clinical applications, load-bearing implant applications of hydroxyapatite (HA) remain problematic due to its intrinsic property limitations. Recent findings of the promising biocompatibility of graphene imply the possibilities of it being potentially used as additives for HA-based composites with enhanced mechanical properties. Here we report HA–reduced graphite oxide nanocomposites synthesized by a liquid precipitation approach followed by spark plasma sintering consolidation. The reduced graphite oxide (rGO) consisted of 2–6 layers of graphene. Rod-like HA grains with the dimensions of ~9 nm in diameter and 20–45 nm in length exhibited oriented nucleation and epitaxial growth on graphene flakes. The (300) plane of HA crystals formed a coherent interfacial bond with the graphene wall and the section of the graphene sheet built a strong interface with the (002) plane of HA crystals. These structural features gave rise to enhanced densification and precluded grain growth of HA in the spark plasma sintered pellets. Fracture toughness of the HA–rGO composites reached 3.94 MPa $m^{1/2}$, showing a 203% increase compared to pure HA. Crack deflection, crack tip shielding and crack bridging at the HA–rGO interfaces were disclosed as the major strengthening regimes in the composites. The enhanced mechanical properties together with the improved proliferation and ALP activity of the human osteoblast cells suggest a great potential of the composites for biomedical applications.

1 Introduction

Hydroxyapatite (HA) has been successfully utilized in orthopedic surgery for promoting fast fixation of bony tissues owing to its similarity in chemistry to human skeletal bone. Allowing direct apposition of host bony tissue, good osteoconductive and osteoinductive capabilities offer HA a great advantage in clinical applications.[1–5] However, the intrinsic brittleness and low fracture toughness of bulk HA are still major hurdles that impede its long-term functional service after clinical surgery under load-bearing conditions.[5,6] Mechanical performances of HA can be improved by incorporating second phase reinforcements like polymers,[7–9] ceramics,[10,11] carbon nanotubes,[12,13] *etc.* Yet few of the materials that have been attempted for HA-based composites satisfy both favorable biocompatibility and sufficient strength. Preferable addition of biocompatible materials favors biological performances of HA. However, the extent to which the mechanical strength is enhanced is usually not sufficient to meet the need of high load-bearing implants.[11] Searching for novel materials without sacrificing the mechanical and biological properties of HA has been a research focus in recent decades. Carbon nanotubes-reinforced HA composites were developed and significantly enhanced fracture toughness and biological performances have been reported.[12,13] However, potential toxicological risk is still a big concern for carbon nanotubes for potential biomedical applications, even though interesting progress has been made on alleviating the toxicity by, for example, competitive bindings of blood proteins.[14,15] As an alternative novel material, graphene has been attracting intense attention due to its unique structural features and exceptional mechanical properties. Biomedical application is one of the exciting opportunities of graphene that inspired the research community to explore it extensively.[16–21] Of particular interest are graphene-based nanomaterials and their biotechnological investigations.[22–28] Graphene and its derivatives further showed the capability of being functionalized with avidin–biotin,[27] peptides,[27,28] NAs,[29,30] proteins,[24,31–34] aptamers,[27,35] small molecules,[27,36] bacteria,[27] and cells,[27,37] suggesting the possibilities of them being employed for building up biological platforms, biosensors and biodevices. Fluorescence resonance energy transfer biosensors based on graphene were reported for sensing the substances ranging from small molecules and DNA to proteins and cells.[29–36,38–41] In contrast to

Ningbo Institute of Materials Technology and Engineering, Chinese Academy of Sciences, Ningbo 315201, China. E-mail: lihua@nimte.ac.cn; Fax: +86-574-86685159; Tel: +86-574-86686224

† Electronic supplementary information (ESI) available. See DOI: 10.1039/c3tb00531c

carbon nanotubes, graphene can be synthesized in a relatively pure environment, which reduces the risk of impurity-induced toxicity. In the light of available scientific evidence pertaining to its biological performances, graphene might potentially be a good candidate for HA-based composites for biomedical applications. Synthesis of HA–graphene powders and fabrication of the bulk composites are yet to be systematically explored.

Nanotechnology is predominately directing the research of biomedical materials for attaining both sufficient mechanical properties and excellent biological performances. Significantly enhanced mechanical strength together with favorable biocompatibility has been achieved for nano-sized HA (nano-HA).[4,42,43] Compared to conventional HA, nano-HA accomplished faster osteoblast proliferation and enhanced osteoclast activity of osteoblast cells on them.[44,45] The development of nanoparticles has been accompanied by the need for a suitable processing technique to retain the fine grain size in bulk materials. Due to simultaneous application of pressure, electrical current and rapid heating rate, spark plasma sintering (SPS) offers better densification of nanoceramic particles at a lower temperature and in a much shorter duration (generally a few minutes) than conventional sintering techniques.[46–48] Studies have shown that SPS processed HA enhanced osteoblast cell proliferation as compared to conventionally sintered HA, proving SPS to be an appropriate technique for consolidating HA for biomedical applications. In this study, HA–reduced graphite oxide composite powders were synthesized *via* a wet chemical approach. The HA–reduced graphite oxide composites were further consolidated by SPS processing. Microstructure characterization revealed oriented nucleation and epitaxial growth of HA nanograins on graphene sheets. Even distribution of the nano-sheets with 2–6 layers of graphene in the SPS HA-based pellets significantly enhanced the mechanical properties and osteoblast attachment and proliferation, shedding light on potential biomedical applications of the novel composites.

2 Materials and methods

2.1 Synthesis of graphene and HA–graphene composites

Large-scale reduced graphite oxide (rGO) was chemically synthesized from high purity flakey graphite. Graphite oxide was prepared by oxidation and exfoliation of graphite *via* the modified Hummer's method.[49,50] Reduction of graphite oxide was subsequently carried out by thermal reduction processing at 200 °C for 30 min in a vacuum (0.1 Pa). The as-received rGO was ultrasonically dispersed in 50 ml ultra-pure water for 120 h in a bath sonicator with an ultrasound power of 300 W. 0.25 mol $Ca(NO_3)_2 \cdot 4H_2O$ was then added into the as-obtained rGO solution, followed by slow addition of 0.15 mol/50 ml $NH_4H_2PO_4$ solution and adjustment of the pH value to 11 using $NH_3 \cdot H_2O$. The mixed solution was mechanically stirred for 2 h and left overnight to settle. The wet chemical approach for synthesizing HA was based on the following chemical reaction:

$$6(NH_4)_2HPO_4 + 10Ca(NO_3)_2 + 8NH_3 \cdot H_2O \rightarrow Ca_{10}(PO_4)_6(OH)_2 + 20NH_4NO_3 + 6H_2O$$

After complete reaction, the resulting slurry was washed centrifugally with distilled water to remove ammonium hydroxide completely and dried at 120 °C. By accurately weighing the rGO and controlling the stoichiometric synthesis of HA, the HA–rGO composite powders with different contents of rGO (0, 0.1 wt%, and 1.0 wt%) were typically produced.

2.2 SPS consolidation

The HA–rGO composites were further consolidated by SPS using a graphite die (Sumitomo Coal Mining SPS system, DR SINTER Model 1050, Japan). The sintering was carried out at 950 °C under a pressure of 30 MPa and a processing time of 3 min in a vacuum (~5 Pa). The HA and HA–rGO pellets were 12 mm in diameter and ~4 mm in thickness.

2.3 Characterization of microstructures

Microstructures of the rGO, HA and HA–rGO powders and SPS pellets were characterized by transmission electron microscopy (TEM, FEI Tecnai F20, the Netherlands) and field emission scanning electron microscopy (FESEM, FEI Quanta FEG250, the Netherlands). Observation of the HA–rGO interface in near-atomic-scale was carried out under a high resolution transmission electron microscope (HRTEM). For the TEM characterization, the specimen preparation involved transferring the powder suspension in ethanol to the micro grids and letting the solvent evaporate. The number of graphene layers was comprehensively characterized by HRTEM and Raman spectrum (Renishaw inVia Reflex, Renishaw, Britain). Phase composition of the samples was analyzed by X-ray diffraction (XRD, D8 Advance, Bruker AXS, Germany) using CuKα radiation ($\lambda = 1.5406$ Å) operated at 40 kV and 40 mA. The goniometer was set at a scan rate of $0.033^\circ\ s^{-1}$ over a 2θ range of 20–60°. Fourier transform infrared spectroscopy (FTIR, Nicolet 6700, Thermo Fisher Scientific, USA) detection was also conducted. The infrared spectrum with a resolution of 4 cm and a scan number of 8 was measured with a spectral region from 400 to 4000 cm^{-1}.

2.4 Assessment of mechanical properties

Fracture toughness (K_{IC}) of the SPS HA–rGO pellets was determined by using the indentation approach.[51] 1000 gf Vickers load was applied on the polished pellets with a loading time of 10 s. A total of 10 points were collected for each sample. The test was conducted on a Micro-Vickers microhardness tester (HV-1000, Shanghai Lianer Testing Equipment Corporation, China). The elastic modulus of the HA and HA–rGO composites was measured by the nanoindentation test carried out using a nanomechanical test system (NANO G200, MTS, USA). The maximum indentation depth chosen for the present test was 1 μm. At least ten indentations were made for an average value for each sample.

2.5 Cell culture test

Attachment, proliferation and differentiation of human osteoblast cells (HFOB 1.19 SV40 transfected osteoblasts) on the HA–rGO composites were examined. Five specimens for each type of

the samples were used for each test condition. Prior to the *in vitro* experiments, the cells were cultured in α-minimum essential medium (α-MEM) (SH30265.01B, HyClone, USA) supplemented with 10% heat-inactivated fetal bovine serum, 100 U ml^{-1} penicillin and 100 μg ml^{-1} streptomycin in an atmosphere of 100% humidity and 5% CO_2 at 37 °C. The cells were seeded at 1×10^4 cells per ml in 96-well culture plates with 200 μl media contained in each well. Proliferation of the cells cultured on the sterilized pellets (1 cm in diameter) was analyzed using the methyl thiazole tetrazodium (MTT) assay. An MTT stock solution of 5 mg ml^{-1} (Sigma, St Louis, MO, USA) was prepared by dissolving MTT in PBS, filtered through a 0.2 μm filter and stored at 4 °C. Then the 96-well plate was removed from the incubator and 20 μl MTT stock solution was added to each well. Cells were incubated for 4 h at 37 °C in an atmosphere of 100% humidity and 5% CO_2. After the incubation, the MTT solution was removed and replaced with 100 μl DMSO. The plate was rotated for 5 min to distribute it evenly at room temperature, and then was read using 490 nm wavelength on a microplate reader machine (spectra max 190, MD, USA). For each type of the pellets, three samples were tested to get an average value and each sample was read three times. For FESEM observation of the cells adhering on the surfaces of the samples, the cells after 24 h incubation were fixed in 2.5% glutaraldehyde for 24 h, dehydrated gradually and coated with gold. Differentiation of the cells cultured on the samples was assessed by measuring their alkaline phosphatase (ALP) activity. The cells (1×10^4 cells per ml) were seeded on the specimens and cultured for 7 days. They were washed twice with PBS and lysed by three cycles of a freezing and thawing program. The as-received aliquots of supernatants were subjected to ALP activity and protein content measurement by using an ALP kit and a micro-Bradford assay kit (Nanjing Jiancheng Biological Engineering Institute, China). The absorbance of the reaction product, *p*-nitrophenol, was measured at the wavelength of 405 nm on the microplate reader machine.

3 Results and discussion

3.1 Characteristics of the synthesized rGO and HA–rGO composites

The as-received rGO standing on the copper grid shows wrinkled-paper-like morphology (Fig. 1a). Further structural characterization by Raman spectroscopy demonstrates almost exclusive presence of graphene sheets in the sample (Fig. 1c). For comparison purposes, the Raman spectrum of the pristine flakey graphite is also shown. The first-order spectra of the pristine graphite and graphene sheets are suggested by the G band at 1580 cm^{-1} and 1583 cm^{-1}, and the D band at 1333 cm^{-1} and 1329 cm^{-1}, respectively. The second-order (two-photon) spectra at 2678 cm^{-1} and 2647 cm^{-1} refer to the 2D band of the graphite and rGO samples. As noticed from the spectrum of the synthesized rGO (Fig. 1c), the intensity ratio of D peak to G peak increases dramatically in comparison with that of the starting graphite (1.16 *vs.* 0.38), implying that the chemical oxidation and thermal reduction processes have introduced considerable structural disorder in the graphene lattice. It has been acknowledged that the Raman spectrum could be used to assess the quality of graphene and determine the number of graphene sheets by the position of the 2D peak,[52] that is, the 2D peak shifts to lower wavenumber values for the rGO with a lower layer number of graphene. TEM observation (Fig. 1a) and FESEM images (data not shown) of the as-received rGO show that the size of the as-received rGO is around 1–2 μm, and the majority of the rGO consist of 2–6 layers of graphene as determined by the Raman spectroscopy measurements and HRTEM observation provided in the later part (Fig. 2c).

The TEM image of the synthesized HA showed a rod-like shape for the HA nanoparticles (Fig. 1b). Further XRD analysis of the HA–rGO composites suggests the presence of crystalline HA and no trace of graphite or graphene oxide was detected (see Fig. S1 in the ESI†). The broad peaks indicate the state of HA as ultrafine nano-crystalline or being with lower crystallinity. The XRD diffraction peaks for rGO are not seen, most likely due to the fact that the monolayer structure of rGO exhibits irregular arrays of atoms in three dimensions. Instead, refined detection by FTIR (Fig. 1d) verified the presence of graphene sheets in the composites by the clear appearance of the absorption bands of methylene groups (CH_2), which are inherent to rGO during the synthesis in this study, at around 2853 cm^{-1} and 2926 cm^{-1}. The C=O stretching band at 1720 cm^{-1} is apparent for rGO on the curve for the starting rGO. Characteristics of graphene sheets were further evidenced by XPS detection (data not shown). The absorption bands at 1044 cm^{-1}, 962 cm^{-1}, 566 cm^{-1} and 475 cm^{-1} are attributed to characteristic absorption of PO_4^{3-} in HA. The band at 3572 cm^{-1} corresponds to the structural OH^- group.[1]

Further TEM observation revealed that rod-like HA nanograins intimately attach to graphene flakes (Fig. 2a). HA grains have the size of ~20 to 45 nm in length and ~9 nm in diameter. The SAD pattern exhibited the typical polycrystalline diffraction pattern of HA (Fig. 2b). In addition, faint six-fold symmetry and polycrystalline diffraction pattern of graphene are also observed (Fig. 2b). The SAD pattern for graphene has been discussed elsewhere,[53–55] which is due to the overlapping or folding together randomly of graphene in the HA–rGO composite powders. The interface between HA grains and graphene platelets was examined by HRTEM observation as per Fig. 2c. There is no obvious evidence indicating the chemical reaction between HA and graphene sheets at their interfaces. It is instead very likely that HA and graphene sheets are connected by van der Waals bonding. Nucleation of HA crystals probably originates on either the graphene wall or the cross-section of graphene multi-sheets, followed by subsequent crystal growth along or perpendicular to the surface of the graphene sheet. Surprisingly, Fourier transform (FFT) and inverse-FFT (IFFT) analyses of the HRTEM images acquired at the HA–rGO interfaces disclosed crystallographic orientation (Fig. 2c), that is, HA grains grow along the (211) plane and exhibit a lattice spacing of 0.282 nm. The (211) plane, along which HA crystals preferentially grow, and the surface of graphene walls form an angle of 27°. For HA crystals, the angle between the planes (300) and (211) of HA is 25°.[1,56] The above finding implies that the (300) plane of HA crystals is very likely parallel to the surface of

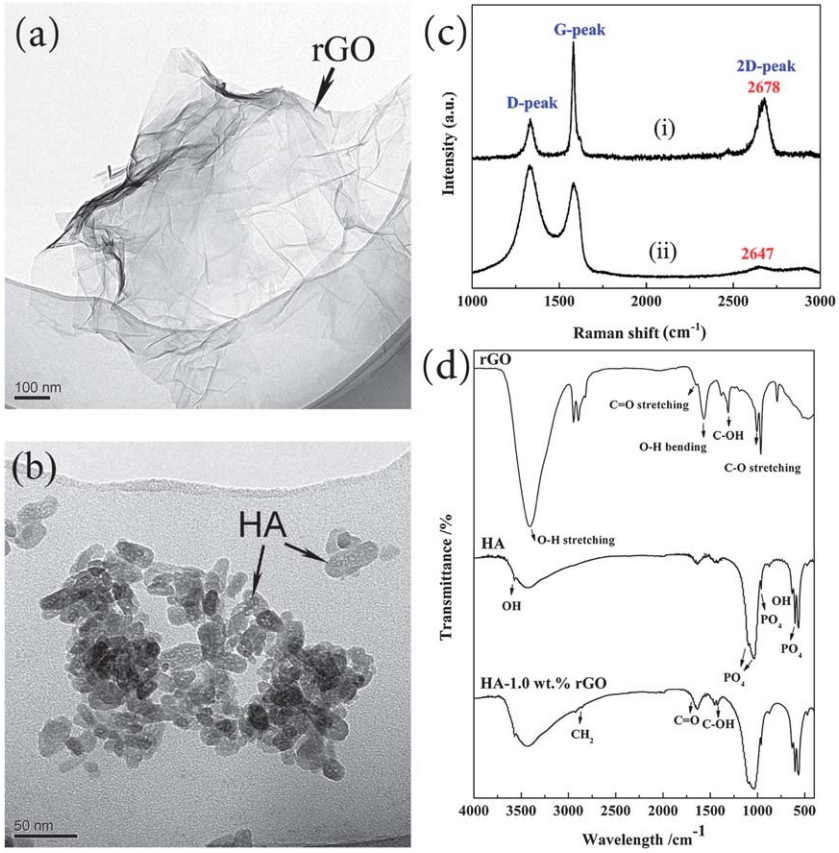

Fig. 1 TEM images and structure analyses of the synthesized rGO and HA–rGO composites, (a) TEM image of rGO showing wrinkled-paper-like morphology, (b) TEM image of HA particles synthesized *via* the wet chemical approach showing rod-like nanostructures, (c) Raman spectrum of rGO (ii) in comparison to that of graphite (i) indicating the exclusive presence of graphene sheets in the synthesized sample, and (d) FTIR spectra of the rGO, pure HA and HA–1.0 wt% rGO composites.

graphene walls. According to the atomic structure of HA,[1] its (300) plane contains Ca(II) atoms at each corner of the rectangle and the distance between each pair of Ca(II) atoms is 0.9418 nm and 0.6884 nm, whereas the distance between two neighboring Ca(I) atoms in plane (100) is 0.9418 nm and 0.3442 nm, respectively. In addition, it was revealed by HRTEM that the distance between adjacent graphene sheets is 0.347 nm. In fact, single layer graphene is constituted by carbon atoms arranged periodically in a hexagonal manner, and the nearest distance between two carbon atoms is 0.142 nm. Multilayer graphene sheets contain several graphene monolayers with the inter-wall distance of 0.34 nm.[57–61]

Based on the above results, a schematic diagram is depicted illustrating the planes (300) and (100) of HA superimposing on the surface of the graphene sheet (Fig. 3a). It has been well established that HA crystallizes in a hexagonal system with the cell parameters $a = b = 9.418$ Å and $c = 6.884$ Å. The HA structure is formed by a tetrahedral arrangement of phosphates (PO_4^{3-}), which constitute the skeleton of the unit cell. Within the unit cell, phosphates are divided into two layers with the heights of 1/4 and 3/4, respectively, resulting in the formation of two types of channels along the *c* axis as denoted by A and B. The walls of channel A are occupied by oxygen atoms from the phosphate group and calcium ions (calcium ions type II – Ca(II)), consisting of two equilateral triangles rotated 60 degrees relative to each other, at the heights of 1/4 and 3/4 respectively. Channel B is occupied by other ions of calcium (calcium ions type I – Ca(I)). In each cell there are two such channels, each of which contains two calcium ions at heights 0 and 1/2.[1] During the synthesis of HA in the presence of graphene sheets, HA crystals preferably align on the graphene surface following a minimum atomic distance mismatch. Along one side of the (300) plane of HA, the distance between the carbon atoms nearest to the Ca(II) atoms is 0.984 nm (between C2 and C3, Fig. 3a). As the distance between the matching Ca(II) atoms on the (300) plane of HA is 0.9418 nm, the mismatch (δ) between the interatomic distance of these two pairs of C and Ca atoms is ~0.04. Moreover, along the vertical direction, the distance between two carbon atoms, coinciding with the Ca(II) atoms of the superimposed (300) plane of HA, is ~0.71 nm. As such, the mismatch (δ) between the two superimposed pair of Ca (in HA) and Ca(II) atoms is 0.03. The mismatch (δ) along both directions is much lower than the incoherence limit of 0.25. Similarly, in the case of the (100) plane of HA crystals, the matching condition in the horizontal direction is the same as that for the (300) plane. However, along the *c*-axis direction, the distance between two Ca(I) atoms in the (100) plane is 0.3442 nm. The distance between carbon atoms most close to it is 0.284 nm. Although the mismatch between two superimposed pairs of Ca and C atoms is ~0.21, which is lower than the incoherence limit of

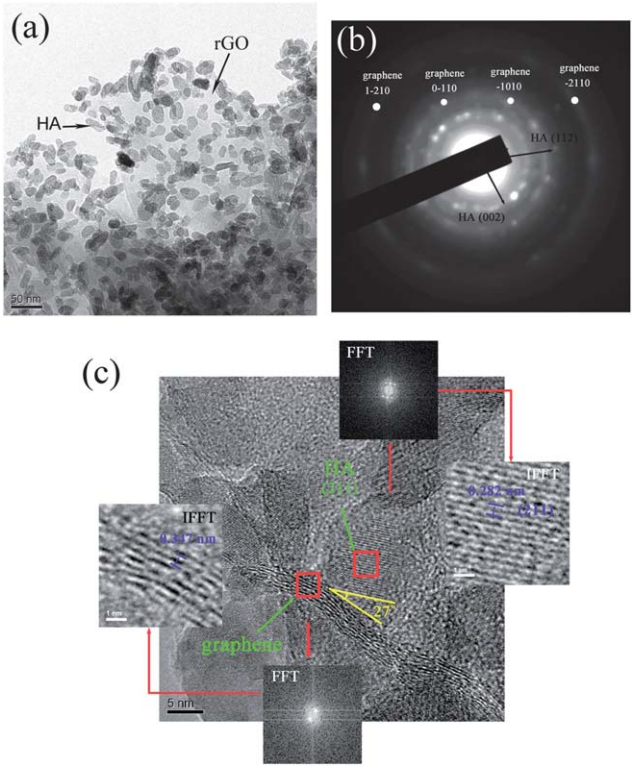

Fig. 2 TEM micrographs of the synthesized HA–rGO composite powders, (a) TEM image shows rod-like HA nanograins with the size of ~20 to 45 nm in length and ~9 nm in diameter adhering to graphene flakes with an intimate contact, (b) SAD pattern evidences the presence of graphene and nano-HA (the faint diffraction rings of graphene were highlighted by the strong white dots), and (c) HRTEM image of the composite powders showing HA–graphene interfaces and FFT and IFFT analyses further reveal the lattice spacing of graphene nanosheets and HA at the interface and preferred orientation of HA crystals on graphene sheets.

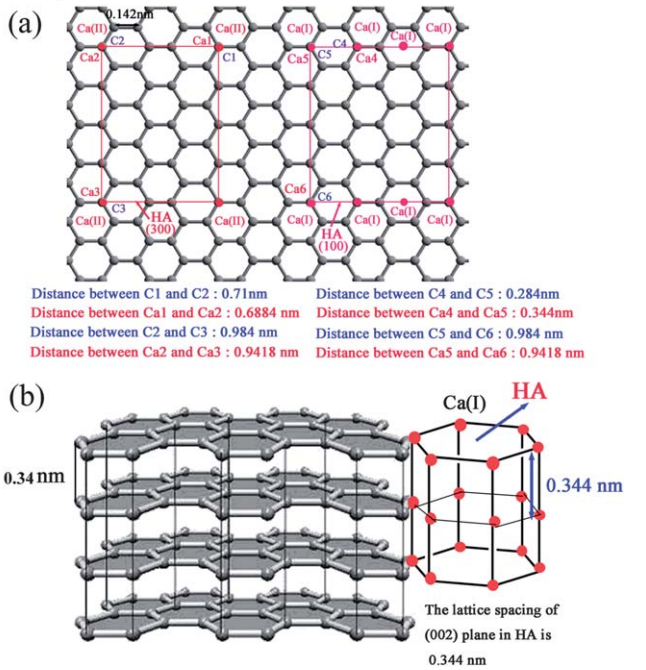

Fig. 3 Schematic illustration of the matched atomic arrangement at (a) the interface between the planes (300) and (100) of HA and the graphene surface, and (b) the interface between the (002) plane of HA and cross-section of graphene sheets.

0.25, it increases the lattice strain compared with that for the (300) plane. Similar research on the interface of HA–CNT composites showed that the (211) plane of HA preferentially matches with CNT walls and the mismatch (δ) between the interatomic distance of C and Ca atoms is 0.09.[12] Our study demonstrates that during the synthesis, the (300) plane of HA can naturally form a stronger and coherent interfacial bond with the graphene wall, as suggested by the relatively smaller lattice mismatch (0.03).

The schematic depiction shown in Fig. 3b illustrates the matching state of the cross-section of graphene nanosheets with the (002) plane of HA crystals. At the cross-section of graphene flakes, the multilayer walls are exposed with an inter-wall spacing of 0.34 nm. The lattice spacing of the (002) plane of HA is 0.344 nm. The lattice mismatch (δ) between the (002) plane of HA crystals and graphene walls is 0.01, which is obviously much lower than the incoherence limit of 0.25, suggesting a strong bond between graphene at its cross-section and HA crystals. Good interfacial bonding can be achieved by small lattice mismatch ($\delta < 0.25$) which gives rise to minor lattice strain.[62] Absence or a small measure of lattice strain in turn improves interfacial adhesion, which further enhances fracture energy of the interfaces. In this study, during the synthesis of HA, its (300) plane takes priority over the (100) plane to match with the surface of graphene sheets. The open ends of graphene multisheets form relatively stronger interfaces with the (002) plane of HA crystals than other planes like (211). The strong and coherent interfaces are essentially the key for achieving competitive mechanical properties of the HA–rGO composites.

3.2 Characteristics of the HA–rGO pellets

Further consolidation by SPS of the synthesized powders has accomplished dense structures of the HA and HA–rGO composites, which can be clearly seen from the SEM image of fractured surfaces of the HA–rGO pellets (see Fig. S2 in the ESI†). Graphene sheets are homogeneously dispersed in the HA matrix with the length of 1–2 μm, showing comparable sizes to the starting nanosheets. Possible fluctuation in curvature in the sub-micron-scale of the nanosheets in the SPS pellets needs further investigation. A close view of the structure by TEM shows a dense interface between graphene sheets and HA grains (Fig. 4a). The fractured surface of the pure HA pellet displays intergranular fracture mode, and the grain size of 1.5–2 μm is easily identified (see Fig. S2 in the ESI†). In contrast, the HA grains in the SPS HA–rGO composites show even grain size ranging from ~100 to 200 nm, as exhibited in the TEM image (Fig. 4a). The addition of rGO makes the sizes of the HA grains smaller. Due to the fast consolidation feature of SPS, taking into account the processing temperature of 950 °C and the short processing duration of 3 min, the majority of HA did not melt (melting point of HA is 1670 °C). However, according to the working principle of SPS, melting at the contact areas between HA grains very likely takes place during the rapid sintering,

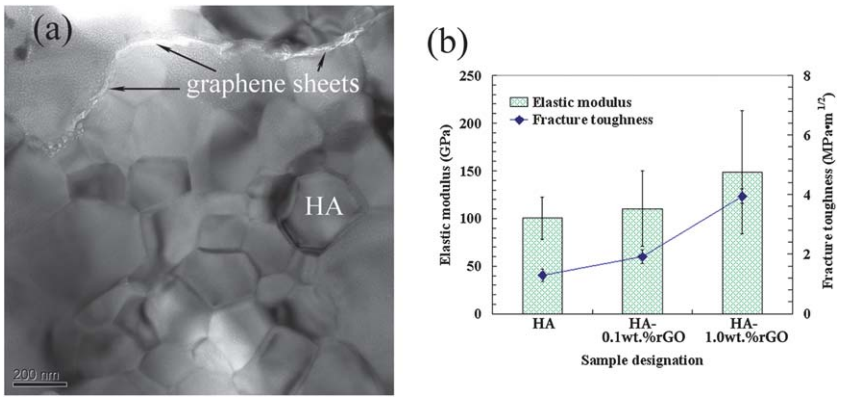

Fig. 4 TEM image showing intact graphene nano-sheets in the SPS HA–rGO pellets (a), and the addition of rGO significantly improved fracture toughness and elastic modulus of the SPS HA–rGO pellets (b).

which is mainly responsible for the grain growth of HA. In addition, grain growth of HA also occurs at elevated temperatures,[4] even though HA did not reach the melt state. As discussed in the earlier part, HA crystals nucleated on the graphene sheet and grew along the sheet with preferred orientation. It is speculated that graphene sheets stimulate nucleation of HA during its recrystallization at elevated SPS processing temperatures, which in turn effectively inhibits grain growth of HA along at least one direction, resulting in finer HA grain sizes. Furthermore, the presence of graphene sheets isolates contact of a certain amount of HA grains, in turn inhibiting effectively the grain growth of HA. Phase analysis shows increased HA crystallinity (as indicated by the sharpened peaks) in the SPS HA and HA–rGO composites (see Fig. S3 in the ESI†). Part of HA has partially decomposed to β-tri-calcium phosphate (β-TCP). HA is a non-conducting ceramic with a poor thermal conductivity of 1.25 W m^{-1} K^{-1} (ref. 63) and electrical conductivity of 7×10^{-7} S cm^{-1}.[64] Since the graphite die is in contact with the surface of the sample, a thermal gradient is created between the internal and external regions, resulting in a non-uniform microstructure, as suggested by the XRD analyses. Addition of rGO, a material with high thermal conductivity and good electrical conductivity, unsurprisingly increased the effective electrical conductivity and in turn reduced the electrical field gradient of the HA-based composites. A very high temperature may be attained within the surface region of the SPS HA sample over the decomposition temperature of HA, usually higher than 1000 °C,[65] leading to localized decomposition.

Microhardness values of the SPS pellets increased from 349 ± 37 Hv for the pure HA to 398 ± 43 Hv for the HA–0.1 wt% rGO and 439 ± 62 Hv for the HA–1.0 wt% rGO pellets. The elastic modulus and fracture toughness of the HA–rGO pellets as a function of the content of rGO in the composites are shown in Fig. 4b. The elastic modulus values of the specimens increase with the increase of rGO content in the composites; the hardness and elastic modulus of the HA–rGO composites are augmented by 25.8% and 47.6%, respectively. It is noted that the indentation-induced cracks are clear in the pure HA pellet, in contrast, however, there is slight cracking produced in the HA–1.0 wt% rGO composite under the same load conditions (see Fig. S4 in the ESI†). The fracture toughness (K_{IC}) of the HA–1.0 wt% rGO composite reaches 3.94 MPa $m^{1/2}$, showing a 203% improvement compared to the pure HA, which is remarkably higher than the HA-based composites toughened by CNT, YSZ or Ti.[11,12,66,67]

Microstructure characterization has given an insight into the possible strengthening mechanisms by graphene sheets in the HA-based composites. As discussed earlier, addition of rGO resulted in formation of finer HA grains, indicating fine grain strengthening as a possible toughening regime. The ultimate strength (σ_u) of a single-layered graphene sheet is 210 GPa in the

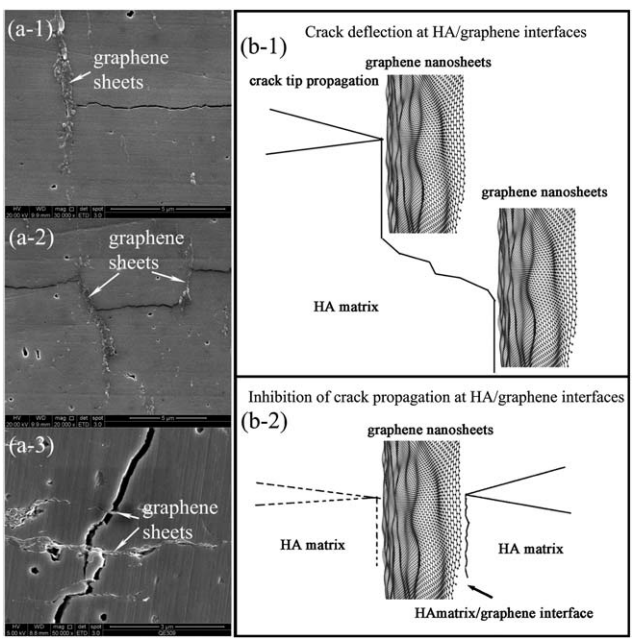

Fig. 5 Inhibition of crack propagation by graphene nano-sheets in the SPS HA–rGO composites. (a) FESEM images showing termination of the crack growth by graphene nano-sheets at the crack tip (a-1), deflection of the crack attained by graphene nano-sheets (a-2) and bridging of the crack by graphene nano-sheets (a-3). The corresponding regimes are schematically illustrated in the right panels (b-1 and b-2).

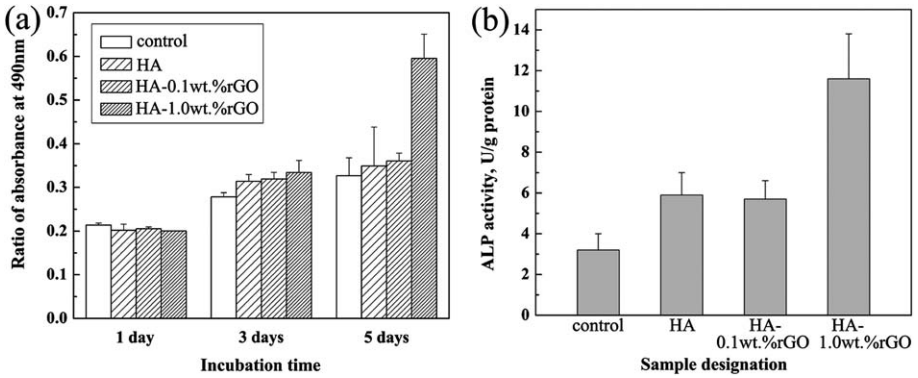

Fig. 6 Cell culture results for the SPS HA–rGO pellets. (a) The osteoblast cells cultured on the pellet surfaces show an enhanced proliferation behavior with an increased content of rGO in the composites. (b) The osteoblast cells proliferated on the surfaces of the pellets show a significantly improved ALP activity as the content of rGO is 1.0 wt% in the composites.

armchair direction and 180 GPa in the zigzag one.[68] The graphene sheets at the crack tip effectively inhibit further growth/propagation of the crack (Fig. 5a-1). Since graphene is a structural analogue of CNT with similar elastic modulus and tensile strength, the interfacial shear strength and reinforcement pullout energy for HA–rGO composites can be estimated based on the model proposed by Chen *et al.* for the Al_2O_3–CNT system.[69] The computed pullout energy for graphene sheets from the HA matrix is 3–40 J m^{-2}, much higher than the fracture energy of monolithic HA, 1 J m^{-2}.[70] Cracks are therefore able to more easily propagate through HA than along the HA–graphene sheet interfaces. In fact, a crack intersects successive graphene sheets and directly deflects to the HA matrix or propagates along the HA–graphene sheet interface and then deflects to the HA matrix (Fig. 5a-2), demonstrating the toughening mechanism of crack deflection. Furthermore, crack bridging offered by graphene sheets is also seen as the cracking is severe (Fig. 5a-3). Individual graphene flakes bridge the gap between the crack surfaces, preventing effectively widening of the crack. The graphene sheets remain intact, providing toughening *via* restraining against the crack tip to open and propagate further. The strengthening regimes associated with the morphological evidence are also schematically depicted and shown in the right panel of Fig. 5. It is obvious that the extent to which the mechanical properties of the HA–rGO composites are enhanced is predominately dependent on the bonding strength of HA–graphene-sheet interfaces. Lahiri *et al.* have investigated the interfacial cohesive strength in HA–CNT and HA–BNNT systems by calculating the pullout energy, and the values of 2–100 J m^{-2} and 1.5–22 J m^{-2} were reported for BNNT and CNT being pulled-out from the HA matrix respectively.[12,56] As mentioned earlier, in our case, the computed pullout energy for the graphene sheets from the HA matrix is 3–40 J m^{-2}. Comprehensive elucidation of the pullout energy is to be reported in another paper.

Apart from the mechanical properties, nontoxicity and favorable biocompatibility of the HA–rGO composites are essential for their potential applications in clinical surgery. Biological performances of the composites were preliminarily examined by a cell culture test in this study. MTT assay shows enhanced proliferation of the osteoblast cells on the rGO-containing HA composites (Fig. 6a). Our finding is consistent with previous research efforts made by other researchers in recent years that graphene films encountered better adherence and proliferation of human osteoblasts and mesenchymal stromal cells on them than on silica.[16] For a better understanding of the effect of rGO on the behavior of the cells, effects of rGO on osteoblast differentiation were herein investigated by alkaline phosphate (ALP) activity assay, which is an early marker of osteoblast differentiation. In the case of ALP activity, the pure HA and the HA–rGO composites had a significantly higher ALP activity than the blank well plate, as shown in Fig. 6b. The ALP expression level on the HA–1.0 wt% rGO composites is about 2 times of that on the pure HA. The unobvious correlation between the graphene dose and the changes in ALP activity could be attributed to different differentiation states of the osteoblast cells, which has been revealed for the osteoblast cells proliferated on CNT.[71,72] It should be noted that the *in vitro* results we reported here are very preliminary and further comprehensive understanding about the biocompatibility of the novel HA–rGO composites is required. Although we should take particular precautions prior to introducing a new material for biological applications and we are still far from a final verdict on the biotoxicity of graphene, the unambiguous evidence provided here already sheds a bright light on the possibility of them being used for load-bearing hard tissue replacement in clinical applications.

4 Conclusions

HA–reduced graphite oxide nanocomposite powders were synthesized by a liquid precipitation approach. Comprehensive microstructural characterization showed that HA nanorods nucleate on and grow along graphene sheets with preferred orientation. The (300) plane of HA forms a naturally strong and coherent interfacial bond with the surface of the graphene wall and the cross-section of graphene builds with the (002) plane of HA crystals a stronger interface due to the smaller lattice mismatch. Bulk HA–reduced graphite oxide pellets have been consolidated by SPS and showed significantly enhanced

mechanical properties and *in vitro* cell behaviors. Fine grain strengthening, graphene flakes pullout on the fracture surface, crack deflection at the HA–graphene interface and crack bridging by graphene sheets were realized to play the key roles in strengthening the composites.

Acknowledgements

We thank Drs Wenge Zheng and Dingding Lu (Ningbo Institute of Materials Technology and Engineering) for technical assistance in synthesis of reduced graphite oxide, Drs Ligen Yu (Nanyang Technological University, Singapore) and Qing Huang and Lu Shen (Ningbo Institute of Materials Technology and Engineering) for technical assistance in spark plasma sintering, and Dr Jinling Xu (Nanyang Technological University, Singapore) for technical assistance in cell culture. This research was supported by National Natural Science Foundation of China (grant # 31271017) and 100 Talents Program of Chinese Academy of Sciences (both to H.L.).

References

1 R. Fazel-Rezai, *Biomedical Engineering – Frontiers and Challenges*, InTech publisher, Rijeka, Croatia, 2011.
2 J. T. Melton, R. Mayahi, S. E. Baxter, M. Facek and C. J. Glezos, *J. Bone Jt. Surg., Br. Vol.*, 2012, **94**, 1067–1070.
3 L. L. Hench and J. M. Polak, *Science*, 2002, **8**, 1014–1017.
4 H. Li, K. A. Khor, V. Chow and P. Cheang, *J. Biomed. Mater. Res., Part A*, 2007, **82**, 296–303.
5 L. G. Yu, K. A. Khor, H. Li and P. Cheang, *Biomaterials*, 2003, **24**, 2695–2705.
6 A. A. White, S. M. Best and I. A. Kinloch, *Int. J. Appl. Ceram. Technol.*, 2007, **4**, 1–13.
7 S. Velayudhan, T. V. Anilkumar, T. V. Kumary, P. V. Mohanan, A. C. Fernandez, H. K. Varma and P. Ramesh, *Acta Biomater.*, 2005, **1**, 201–209.
8 S. Zhou, X. Zheng, X. Yu, J. Wang, J. Weng, X. Li, B. Feng and M. Yin, *Chem. Mater.*, 2007, **19**, 247–253.
9 L. Fang, Y. Leng and P. Gao, *Biomaterials*, 2006, **27**, 3701–3707.
10 J. Li, B. Fartash and L. Hermansson, *Biomaterials*, 1995, **16**, 417–422.
11 Z. J. Shen, E. Adolfsson, M. Nygren, L. Gao, H. Kawaoka and K. Niihara, *Adv. Mater.*, 2001, **13**, 214–216.
12 D. Lahiri, V. Singh, A. K. Keshri, S. Seal and A. Agarwal, *Carbon*, 2010, **48**, 3103–3114.
13 D. Zhang, C. Yi, J. Zhang, Y. Chen, X. Yao and M. Yang, *Nanotechnology*, 2007, **18**, 475102–475111.
14 C. Ge, J. Du, L. Zhao, L. Wang, Y. Liu, D. Li, Y. Yang, R. Zhou, Y. Zhao, Z. Chai and C. Chen, *Proc. Natl. Acad. Sci. U. S. A.*, 2011, **108**, 16968–16973.
15 G. Zuo, S. Kang, P. Xiu, Y. Zhao and R. Zhou, *Small*, 2012, DOI: 10.1002/smll.201201381.
16 M. Kalbacova, A. Broz, J. Kong and M. Kalbac, *Carbon*, 2010, **48**, 4323–4329.
17 G. Y. Chen, D. W. Pang, S. M. Hwang, H. Y. Tuan and Y. C. Hu, *Biomaterials*, 2012, **33**, 418–427.
18 T. R. Nayak, H. Andersen, V. S. Makam, C. Khaw, S. Bae, X. Xu, P. L. R. Ee, J. H. Ahn, B. H. Hong, G. Pastorin and B. Ozyilmaz, *ACS Nano*, 2011, **5**, 4670–4678.
19 N. Li, X. M. Zhang, Q. Song, R. G. Su, Q. Zhang, T. Kong, L. W. Liu, G. Jin, M. L. Tang and G. S. Cheng, *Biomaterials*, 2011, **32**, 9374–9382.
20 H. N. Lim, N. M. Huang, S. S. Lim, I. Harrison and C. H. Chia, *Int. J. Nanomed.*, 2011, **6**, 1817–1823.
21 W. Paul and C. P. Sharma, *Trends Biomater. Artif. Organs*, 2011, **25**, 91–94.
22 S. Kim, S. H. Ku, S. Y. Lim, J. H. Kim and C. B. Park, *Adv. Mater.*, 2011, **23**, 2009–2014.
23 H. Fan, L. Wang, K. Zhao, N. Li, Z. Shi, Z. G. Ge and Z. X. Jin, *Biomacromolecules*, 2010, **11**, 2345–2351.
24 Y. Y. Shao, J. Wang, H. Wu, J. Liu, I. A. Aksay and Y. H. Lin, *Electroanalysis*, 2010, **22**, 1027–1036.
25 M. Pumera, A. Ambrosi, A. Bonanni, E. L. K. Chng and H. L. Poh, *TrAC, Trends Anal. Chem.*, 2010, **29**, 954–965.
26 T. Kuila, S. Bose, P. Khanra, A. K. Mishra, N. H. Kim and J. H. Lee, *Biosens. Bioelectron.*, 2011, **26**, 4637–4648.
27 Y. Wang, Z. H. Li, J. Wang, J. H. Li and Y. H. Lin, *Trends Biotechnol.*, 2011, **29**, 205–212.
28 T. H. Han, W. J. Lee, D. H. Lee, J. E. Kim, E. Y. Choi and S. O. Kim, *Adv. Mater.*, 2010, **22**, 2060–2064.
29 C. H. Lu, H. H. Yang, C. L. Zhu, X. Chen and G. N. Chen, *Angew. Chem., Int. Ed.*, 2009, **48**, 4785–4787.
30 H. J. Jang, Y. K. Kim, H. M. Kwon, W. S. Yeo, D. E. Kim and D. H. Min, *Angew. Chem., Int. Ed.*, 2010, **49**, 5703–5707.
31 J. L. Zhang, F. Zhang, H. J. Yang, X. Huang, H. Liu, J. Y. Zhang and S. W. Guo, *Langmuir*, 2010, **26**, 6083–6085.
32 Y. Ohno, K. Maehashi, Y. Yamashiro and K. Matsumoto, *Nano Lett.*, 2009, **9**, 3318–3322.
33 P. Laaksonen, M. Kainlauri, T. Laaksonen, A. Shchepetov, H. Jiang, J. Ahopelto and M. B. Linder, *Angew. Chem., Int. Ed.*, 2010, **49**, 4946–4949.
34 J. B. Liu, S. H. Fu, B. Yuan, Y. L. Li and Z. X. Deng, *J. Am. Chem. Soc.*, 2010, **132**, 7279–7281.
35 Y. Lu and J. W. Liu, *Curr. Opin. Biotechnol.*, 2006, **17**, 580–588.
36 Y. Q. Wen, F. F. Xing, S. J. He, S. P. Song, L. H. Wang, Y. T. Long, D. Li and C. H. Fan, *Chem. Commun.*, 2010, **46**, 2596–2598.
37 C. X. Guo, X. T. Zheng, Z. S. Lu, X. W. Lou and C. M. Li, *Adv. Mater.*, 2010, **22**, 5164–5167.
38 P. R. Selvin, *Nat. Struct. Biol.*, 2000, **7**, 730–734.
39 S. J. He, B. Song, D. Li, C. F. Zhu, W. P. Qi, Y. Q. Wen, L. H. Wang, S. P. Song, H. P. Fang and C. H. Fan, *Adv. Funct. Mater.*, 2010, **20**, 453–459.
40 N. E. Broude, *Trends Biotechnol.*, 2002, **20**, 249–256.
41 H. F. Dong, W. C. Gao, F. Yan, H. X. Ji and H. X. Ju, *Anal. Chem.*, 2010, **82**, 5511–5517.
42 J. Wang and L. L. Shaw, *Biomaterials*, 2009, **30**, 6565–6572.
43 S. Bose, S. Dasgupta, S. Tarafder and A. Bandyopadhyay, *Acta Biomater.*, 2010, **6**, 3782–3790.
44 T. J. Webster, C. Ergun, R. H. Doremus and R. W. Siegel, *Biomaterials*, 2000, **21**, 1803–1810.
45 T. J. Webster, C. Ergun, R. H. Doremus, R. W. Siegel and R. Bizios, *Biomaterials*, 2001, **22**, 1327–1333.

46 Z. A. Munir and U. Anselmi-Tamburini, *J. Mater. Sci.*, 2006, **41**, 763–777.
47 S. Diouf and A. Molinari, *Powder Technol.*, 2012, **221**, 220–227.
48 X. Guo, J. E. Gough, P. Xiao, J. Liu and Z. Shen, *J. Biomed. Mater. Res., Part A*, 2007, **82**, 1022–1032.
49 M. J. McAllister, J. L. Li, D. H. Adamson, H. C. Schniepp, A. A. Abdala, J. Liu, M. Herrera-Alonso, D. L. Milius, R. Car, R. K. Prud'homme and I. A. Aksay, *Chem. Mater.*, 2007, **19**, 4396–4404.
50 W. S. Hummers Jr and R. E. Offeman, *J. Am. Chem. Soc.*, 1958, **80**, 1339.
51 R. Venkataraman and R. Krishnamurthy, *J. Eur. Ceram. Soc.*, 2006, **26**, 3075–3081.
52 Y. Zhu, S. Murali, W. W. Cai, X. S. Li, J. W. Suk, J. R. Potts and R. S. Ruoff, *Adv. Mater.*, 2010, **22**, 3906–3924.
53 H. Persson, Y. Yao, U. Klement and R. W. Rychwalski, *eXPRESS Polym. Lett.*, 2012, **6**, 142–147.
54 G. Lu, S. Mao, S. J. Park, R. S. Ruoff and J. H. Chen, *Nano Res.*, 2009, **2**, 192–200.
55 J. C. Meyer, A. K. Geim, M. I. Katsnelson, K. S. Novoselov, D. Obergfell, S. Roth, C. Girit and A. Zettl, *Solid State Commun.*, 2007, **143**, 101–109.
56 D. Lahiri, V. Singh, A. P. Benaduce, S. Seal, L. Kos and A. Agarwal, *J. Mech. Behav. Biomed. Mater.*, 2011, **4**, 44–56.
57 L. Pauling, *The Nature of the Chemical Bond*, Cornell University Press, Ithaca, NY, 1960.
58 K. S. Novoselov, D. Jiang, F. Schedin, T. J. Booth, V. V. Khotkevich, S. V. Morozov and A. K. Geim, *Proc. Natl. Acad. Sci. U. S. A.*, 2005, **102**, 10451–10453.
59 K. S. Novoselov, A. K. Geim, S. V. Morozov, D. Jiang, Y. Zhang, S. V. Dubonos, I. V. Grigorieva and A. A. Firsov, *Science*, 2004, **306**, 666–669.
60 M. I. Katsnelson, *Mater. Today*, 2007, **10**, 20–27.
61 C. Lee, X. Wei, J. W. Kysar and J. Hone, *Science*, 2008, **321**, 385–388.
62 D. A. Porter and K. E. Easterling, *Phase Transformation in Metals and Alloys*, CRC Press, Cheltenham, UK, 2001.
63 M. Gaona, R. S. Lima and B. R. Marple, *Mater. Sci. Eng., A*, 2007, **458**, 141–149.
64 A. Laghzizil, N. El Herch, A. Bouhaouss, G. Lorente and J. Macquete, *J. Solid State Chem.*, 2001, **156**, 57–60.
65 J. Zhou, X. Zhang, J. Chen, S. Zeng and K. de Groot, *J. Mater. Sci.: Mater. Med.*, 1993, **4**, 83–85.
66 F. Watari, A. Yokoyama, M. Omori, T. Hirai, H. Kondo, M. Uo and T. Kawasaki, *Compos. Sci. Technol.*, 2004, **64**, 893–908.
67 Q. Chang, D. L. Chen, H. Q. Ru, X. Y. Yue, L. Yu and C. P. Zhang, *Biomaterials*, 2010, **31**, 1493–1501.
68 Z. Ni, H. Bu, M. Zou, H. Yi, K. Bi and Y. Chen, *Phys. B*, 2010, **405**, 1301–1306.
69 Y. Chen, K. Balani and A. Agarwal, *Appl. Phys. Lett.*, 2008, **92**, 011916.
70 A. Nakahira and K. Eguchi, *J. Ceram. Process. Res.*, 2001, **2**, 108–112.
71 L. H. Ding, J. Stilwell, T. T. Zhang, O. Elboudwarej, H. J. Jiang, J. P. Selegue, P. A. Cooke, J. W. Gray and F. F. Chen, *Nano Lett.*, 2005, **5**, 2448–2464.
72 D. W. Zhang, C. Q. Yi, J. C. Zhang, Y. Chen, X. S. Yao and M. S. Yang, *Nanotechnology*, 2007, **18**, 475102.

